

Evolution of stellated gold nanoparticles: new conceptual insights into controlling the surface processes

Gurvinder Singh (✉ gurvinder.singh@sydney.edu.au)

The University of Sydney

Hesamodin Jami

The University of Sydney

Pooria Lesani

The University of Sydney

Shubhayan Bhattacharya

Indian Institute of Technology Madras

Yogambha Ramaswamy

The University of Sydney

Prem B Bisht

Indian Institute of Technology Madras

Hala Zreiqat (✉ hala.zreiqat@sydney.edu.au)

The University of Sydney

Research Article

Keywords: Surface diffusion, shape control, stellated nanoparticles, self-assembly, nanoplasmonics, octapod, stellated octahedron

Posted Date: June 2nd, 2021

DOI: <https://doi.org/10.21203/rs.3.rs-405985/v1>

License: © ⓘ This work is licensed under a Creative Commons Attribution 4.0 International License.

[Read Full License](#)

Version of Record: A version of this preprint was published at Nano Research on August 11th, 2021. See the published version at <https://doi.org/10.1007/s12274-021-3635-1>.

Abstract

Understanding the surface processes (deposition and surface diffusion) that occur at or close to the surface of growing nanoparticles is important for fabricating reproducibly stellated or branched gold nanoparticles with precise control over arm length and spatial orientation of arms around the core. By employing a simple seed-mediated strategy, we investigate the key synthetic variables for precise tuning of in situ surface processes (competition between the deposition and surface diffusion). These variables include the reduction rate of a reaction, the packing density of molecules/ions on the high surface energy facets, and temperature. As a result, the thermodynamically stabilized nanoparticles (cuboctahedron and truncated cube) and kinetic products (cube, concave cube, octapod, stellated octahedron, and rhombic dodecahedron) in different sizes with high quantitative shape yield (> 80%) can be obtained depending on the reduction rate of reaction and the packing density of molecules/ions. With computer simulation, we studied the stability of stellated (branched structure) and non-stellated (non-branched structure) gold nanoparticles at high temperature. We construct a morphology phase diagram by varying different synthetic parameters, illustrating the formation of both stellated and non-stellated gold nanoparticles in a range of reaction conditions. The stellated gold nanoparticles display shape-dependent optical properties and can be self-assembled into highly ordered superstructures to achieve an enhanced plasmonic response. Our strategy can be applied to other metal systems, allowing for the rational design of advanced new stellated metal nanoparticles with fascinating symmetry dependent plasmonic, catalytic, and electronic properties for technological applications.

1. Introduction

Anisotropic gold (Au) nanoparticles (NPs) exhibit exceptional chemical and physical properties by virtue of their size, shape, internal structure, and surface characteristics.[1–6] These unique properties make these anisotropic Au NPs suitable for a range of technological applications, including bioimaging, biosensing, therapeutics, diagnosis and catalysts.[7–9] Furthermore, anisotropic NPs offer several advantages over spherical Au NPs such as enhanced margination,[10, 11] high binding affinity for targeting,[12, 13] prolong blood circulation time,[14] better biodistribution, high cellular uptake, [15–17] enhanced tumor deposition,[18, 19] and improved therapeutic efficacy.[20–22] In the past decades, a number of synthetic strategies have been established for the synthesis of anisotropic Au NPs.[23–29] In particular, a seed-mediated growth has widely been explored for growing anisotropic Au NPs because of its exceptional degree of control over the size, shape, and composition of the NPs via distinct separation of the nucleation event from the growth stage.[23, 30, 31] Examples of shape-controlled synthesis of Au NPs via a seed-mediated approach include spherical, cubes, rods, stars, triangles, tetrahedra, octahedra, wires, bipyramids, and decahedra.[23, 30, 32–34]

Among various anisotropic NPs, symmetrically stellated Au NPs (*e.g.* multipod or octapod) with a single core and several protruding arms with sharp tips are of particular interest because of their excellent localized surface plasmon resonance (LSPR),[24, 35] remarkable enhancement in the local electric field and conversion of light to heat energy at their sharp tips, low cytotoxicity, and higher cellular uptake.[36]

These advantages have boosted the research interest in the controlled synthesis of multipod Au NPs. A seed-mediated co-reduction has been employed to rationally design Au-Pd NPs of octapod with eight-branched.[37] This approach involved the simultaneous reduction of two metallic precursors on pre-formed Au seed particles to grow bimetallic (AuPd) octapod.[38, 39] These Au-Pd octapod NPs cannot be used for biomedical applications because of *in vivo* cytotoxicity of Pd.[40, 41] Recently, an alternative method has been developed for growing Au octapod NPs using a synergistic combination of two reducing agents of ascorbic acid (AA) and 1-methylpyrrolidine.[36] However, this approach suffers from limitations such as size control of Au octapods NPs and morphological inhomogeneity (variation in the length and tip of the arms, including unsymmetrical orientation of arms) in the NP obtained from different batches of synthesis. Despite the progress made so far in the growth of stellated Au NPs, challenge remains in the reproducible synthesis of stellated NPs with precise control over the number, size, and spatial orientation of arms in high yield. In addition, there are a very few studies in the literature that provide in-depth fundamental mechanistic understanding of stellated Au NPs formation due to the number of reaction variables (the role of reducing agent, capping ligands, temperature, and halide ions) involved in the growth reaction add complexity. The formation of stellated NPs with controlled arm length along with their spatial orientation is vital to achieve a smaller plasmon damping and a large local field enhancement using a single wavelength laser excitation for use them in technological applications.”

Here, we demonstrate a simple seed-mediated approach to fabricate stellated Au NPs with uniformity in arm length, tip size and symmetrical orientation of arms in a high yield. This approach employs cetyltrimethylammonium ammonium chloride (CTAC) surfactant, ascorbic acid (AA), and sodium bromide to grow anisotropic stellated Au NPs. We show that precise control over the morphology of Au NPs (from cuboctahedra, truncated cube, cube, concave cube to octapod, stellated octahedron, and rhombic dodecahedron) can simply be obtained by adjusting the different amounts of ascorbic acid (AA) and sodium bromide (NaBr) in the growth solution without altering the CTAC concentration. The size and yield of stellated NPs can also be tuned by varying the concentration of NaBr in the growth solution. An experimental approach combined with computer simulation was employed to illuminate the role of surface process in forming stellated Au NPs. Our detailed investigation highlights the significance of the reduction rate of reaction (regulated by the concentration of AA and NaBr as well as the reaction temperature), which influences the surface processes (*i.e.* deposition of atomic species and their diffusion on the surface). In this work, we construct a morphological phase diagram as a function of NaBr and AA/Au³⁺, revealing the evolution of both thermodynamically and kinetically stabilized reaction products in a range of experimental conditions. Furthermore, we demonstrate the self-assembly of stellated Au NPs into ordered superstructures and their enhanced plasmonic properties.

2. Results And Discussion

A schematic illustration for synthesizing anisotropic Au NPs is shown in Fig. 1. A detailed synthetic protocol is described in the method section. In brief, spherical seeds were prepared by a rapid injection of 20 mM sodium borohydride to aqueous solution of CTAC and HAuCl₄ under vigorous stirring. The seed

solution left undisturbed for 1 hr. Later, CTAC capped spherical seeds (25 μL) were transferred to growth solution A (Fig. 1). When the colour of growth solution (A) turned to light pink, 25 μL of seed solution from the growth solution (A) was immediately transferred to the growth solution (B). The resultant solution was left undisturbed for 20 min at 30°C. The solution was centrifuged twice (2500 rpm) and dispersed the solid residue in deionized water. In the seed-mediated approach, the growth of anisotropic Au NP depends on a number of reaction parameters including, the concentration/amount of reducing agent and halide ions and the concentration of metal precursor and temperature. However, the most direct way to control the seed growth is the concentration of reducing agent (AA).

To investigate how the concentration of AA effects the shape evolution of Au NPs, we varied the volume of 40 mM AA added to the growth solution. When a low amount of 40 mM AA (60 μL) was added to the growth solution, we observed polydispersity in the shape of Au NPs (Fig. 2(a) and Fig. S1 in the ESM). This is due to an incomplete or low reduction rate of Au^{3+} ions (1.9 mmol) by AA (2.4 mmol). For the complete reduction of Au^{3+} ions, the concentration of AA should be twice as the concentration of Au^{3+} ions. To quantitatively determine the shape yield, we analyzed more than 200 NPs from different scanning electron microscopy (SEM) images. We noticed the emergence of cuboctahedra Au NPs with 20% yield as a major reaction product under this condition (Fig. 3(a)). The yield of cuboctahedra Au NPs significantly enhanced to $\sim 89\%$ when the amount of 40 mM AA in the growth solution was increased to 75 μL (Figs. 2(b) and 3(a), and Fig. S2 in the ESM). We observed a change in the shape of Au NP from cuboctahedra to truncated cube as the volume of 40 mM AA increased from 75 μL to 80 μL in the growth solution (Fig. 2(c) and Fig. S3 in the ESM). Here, the quantitative yield of cuboctahedra NP was decreased to $\sim 21\%$ compared to the yield of the truncated cube ($\sim 53\%$) (Fig. 3(a)). The degree of truncation also decreased with the increase in the amount of 40 mM AA (from 80 μL to 90 μL) in the growth solution, and cubic Au NPs with rounded corner were obtained as a primary reaction product (yield $\sim 76\%$) along with notably low yield ($\sim 4\%$) of truncated cube (Figs. 2(d) and 3(a)).

The overgrowth of cubic (growth at the corners) commenced when 95 μL of 40 mM AA was added to the growth solution (Fig. 2(e)). SEM image revealed the presence of overgrown cubic ($\sim 53\%$) and cubic Au NP ($\sim 23\%$) in the reaction mixture (Fig. 3(a)). This suggested that all cubic NP do not overgrow at the same rate. The stellated Au NPs, *i.e.*, octapod (yield $\sim 80\%$) and stellated octahedron (yield $\sim 89\%$) were obtained when 100 μL and 110 μL of 40mM AA was added to the growth solution (Figs. 2(f), (g), Fig. 3(a), and Figs S4 and S5 in the ESM). The formation of stellated Au NPs resulted from the continued growth at the corners of the cubic NP. It should be noted that we found a difference in the morphology of octapod and stellated octahedron. An octapod NP is formed from the protrusion of eight arms from the core of NP. A stellated octahedron is the stellation of the octahedron, which is built by placing eight tetrahedra on each face of octahedron (Fig. 2(i)). SEM images taken at different view displayed in Fig. 2(j) further confirmed the formation of stellated octahedron Au NP. When the reduction rate was significantly increased by adding 150 μL of 40 mM AA, rhombic dodecahedral Au NP bound by the $\{110\}$ facets in high yield ($\sim 88\%$) were formed (Fig. 2(h) and Fig. 3(a)). In highly supersaturated solution (high reduction rate), an accelerated growth along the $\langle 100 \rangle$ and $\langle 111 \rangle$ directions (because of the low packing density of

CTAC molecules on the {100} and {111} facets) guided the formation of rhombic dodecahedra Au NP enclosed by 12 {110} high energy facets. Our results suggested that a progressive increase in the amount of AA in the growth solution leads to morphological evolution from cuboctahedra to cube, octapod, stellated octahedra, and finally, rhombic dodecahedra.

The synthesis mechanism of anisotropic Au NPs involved three steps in the seed-mediated process. In the first step, CTAC capped Au seed particles (size: 2 ± 1 nm) formed (Fig. S6 (a) in the ESM). A detailed structural HRTEM analysis performed by Walsh *et al* revealed the single crystalline nature of Au seed particles synthesized using a similar procedure.[42] Furthermore, the visual appearance of CTAC capped Au seed solution (brown colour) is similar to synthesized CTAB capped Au seed solution, suggesting no significance difference in seed particles capped by CTAC and CTAB (Fig. S7 in ESM). In the second step, CTAC capped Au seed particles introduced to the first growth solution. The colour of the solution turned to light pink colour and red colour after 5s and 15 min of the reaction, respectively (insets in Fig. S6 (b) and (c) in the ESM). This suggested the enlargement of Au seed particles along with time. To study the reaction products from the first growth solution after 5s and 15 min of the reaction, we stopped the reaction by adding PEG-thiol (Poly(ethylene glycol) methyl ether thiol) to the growth solution followed by centrifugating at 10000 rpm. TEM image showed the formation of 11 ± 2 nm Au NPs after 5s (pink colour solution, Fig. S6 (b)) and SEM image revealed Au NPs of size 30 ± 2 nm after 15 min (red colour solution, Fig. S6 (c)). In the third step, the seed particles of size ~ 11 nm from the first solution (light pink colour solution) were added to the second growth solution, thus, facilitating the growth of anisotropic Au NPs. The morphology of Au NPs in the second growth solution is governed by the amount of AA added to the second growth solution. It should be noted that the addition of large size Au seed particles (~ 30 nm) to the growth solution resulted to a low yield of stellated and non-stellated Au NPs. Therefore, we choose optimal size (~ 11 nm) of Au seed particles to fabricate Au NPs in different morphologies.

The reduction rate of reaction plays an important role in achieving thermodynamic and kinetic favourable reaction products because it influences the growth reaction pathways of NPs (*i.e.* diffusion-controlled vs. surface processes). Therefore, it is imperative to establish a relationship between the reduction rate and the morphology of NP (thermodynamic vs. kinetic product). We determined the rate constant (k) of growth reaction by varying amount of 40 mM AA and fitting the absorbance (A)-time (t) profile curves obtained from dynamic ultraviolet-visible (UV-Vis) measurements with the equation (Fig. S10 in the ESM)

$$A = A_{max}(1 - e^{-kt^n})$$

1

where A_{max} is the maximum absorbance of the growth reaction and n is a critical growth exponent.[43] The results displayed in the table 1 showed the increase in the rate constant (k) of the reaction with the increased amount of 40 mM AA in the growth solution (implying the control of the reduction rate of precursor via the amount of AA added to the solution). When a low amount of AA is present in the growth solution, the sluggish reduction rate of the metallic precursor leads to low supersaturation. This results in

a high concentration gradient between the bulk and monomer concentration in the vicinity of growing NP (a low diffusion rate of monomers from bulk to NP surface, *i.e.*, diffusion controlled growth). These conditions favor the evolution of Au NP into different morphologies of low surface energy (thermodynamic Wulff construction).[44] In FCC metal, the surface energy (γ) of different crystallographic facets follows the trend; $\gamma\{110\} > \gamma\{100\} > \gamma\{111\}$.[45] In our experiments, we obtained cuboctahedron Au NPs enclosed by both $\{100\}$ and $\{111\}$ facets with an area ratio of 1: 0.58 at a low reduction rate (Figs. 2(a) and (b)). As the reduction rate was slightly increased by adding 80 μL of 40 mM AA, the surface area of $\{100\}$ facets increase, and the surface area of $\{111\}$ decreases. As a result, truncated cube Au NP formed (Fig. 2(c)). Therefore, the diffusion controlled growth reaction under low supersaturation regime facilitate the fabrication of thermodynamically favourable reaction products (cuboctahedra and truncated cube Au NP).

When the concentration of AA in the growth solution was sufficiently increased, the faster reduction rate led to higher supersaturation (excess concentration of monomers in the growth solution) and the rapid diffusion of monomer units to the growing NP surface. In this case, the surface controlled process dominates, and the shape of Au NPs is governed by kinetic factors, such as the rate of deposition ($V_{deposition}$) and diffusion ($V_{diffusion}$). A balance of deposition rate and diffusion rate ($V_{deposition} = V_{diffusion}$) favoured the formation of Au nanocubes bound by the high surface energy $\{100\}$ facets (Fig. 2(d)). When $V_{deposition} > V_{diffusion}$, the surface diffusion is very sluggish, and thereby, the growth facilitates at the corner of cubic NP (in the $\langle 111 \rangle$ direction). As a result, concave Au nanocubes were obtained (Fig. 2(e)). Further increase in the reduction rate significantly enhances the rate of deposition ($V_{deposition} \gg V_{diffusion}$) and suppresses the surface diffusion ($V_{diffusion}$). The growth under such conditions led to the formation of kinetically favourable products (octapods and stellated octahedra), as shown in Figs. 2(f) and (g).

The surface diffusion is a thermally activated process that can be controlled by the reaction temperature. To elucidate the role of surface diffusion in the formation of stellated Au NPs (octapod and stellated octahedron), we synthesized Au NPs at different temperatures at the fixed volumes of 40 mM AA (95 μL and 110 μL). When the reaction temperature was set to 10°C, Au NPs of cubic morphology formed instead of concave Au NPs (AA = 95 μL) and stellated octahedron (AA = 100 μL) formation at 30°C, indicating the balance deposition rate and surface diffusion at the surface of NP (Figs. S9(a) and (d) in the ESM). Raising the temperature of the growth solution to 70°C and 90°C, we obtained concave cubic and stellated octahedron Au NPs as a major reaction product (Figs. S9 (b), (c), (e) and (f) in the ESM). These morphologies of Au NPs are identical to morphologies of Au NPs obtained at 30°C. From these results, it is clear that the increase in the growth temperature from 30°C to 90°C does not have a significant influence on the surface processes (*i.e.* $V_{deposition} \gg V_{diffusion}$). Furthermore, our results also suggest that the increase in the temperature of growth solution has no significant influence on the packing density of CTAC on the high energy surfaces of Au NPs or the solubility of CTAC surfactant molecules. Therefore, Au NPs of concave cubic, octapod and stellated octahedron morphologies can be synthesized as long as the surface diffusion of atomic species are suppressed, for example, the

temperature range from 30°C to 90°C. At a low temperature (below 30°C), the balance between the surface diffusion and deposition lead to the formation cubic Au NPs.

To investigate the stability of the pre-formed Au NPs of octapod morphology, we employed molecular dynamics simulations under varying thermal conditions. We did not observe the change in the morphology of thermally equilibrated Au octapods at room temperature (Fig. 3(b)). The octapod Au seed at 300 K was heated until the temperature reached 500 K, and the system left in a thermal bath for about 100 ns or more. A very few minor changes can be noticed at the atomic level (not at the macro level) in the Au octapod (Fig. 3(c)). This suggested no significant surface diffusion of atoms on the surface of NPs at both room temperature and 500 K. We then considered to heat up the system until it reached 700 K and left the system to find its final morphology in the thermal bath for 200 ns. In this case, the disappearance of branches in the stellated Au NP indicated the activation of the surface diffusion process, *i.e.*, the migration of Au atoms from branches/arms to fill the gap between the arms. As a result, the morphology of Au NP changed from octapod to rounded cubic as show in Fig. 3(d), indicating a significant increase in the rate of surface diffusion ($V_{\text{diffusion}} \gg V_{\text{deposition}}$). We noticed a further change in the shape of Au NPs to spherical when the system was left at 1350K in the thermal bath for another 450 ns (Fig. 3(e)). These simulation results suggest the stability of octapod morphology of Au NPs at high temperature upto 500K, and the significant increase in the surface diffusion of atomic species above 500 K can cause the change in the morphology of Au NPs, *i.e.*, cubic (700 K) and spherical (1350 K).

To examine how the packing density of molecules/ions around NPs influences the surface processes and, thus, the formation of stellated or non-stellated Au NPs, a surface-sensitive XPS (X-ray photoelectron spectroscopy) technique was used to collect survey and high-resolution XPS spectra from various anisotropic Au NPs shown in Figs. 2(b)-(d) and Figs. 2(f)-(h). The survey spectra showed C, N, O, Cl and Au in all samples (Table S1 in the ESM). However, we did not notice any trace amount of Br ions on the surface of anisotropic Au NPs. The absence of Br⁻ ions on the surface of Au NPs suggested no interaction of Br⁻ ions to the growing NPs (*i.e.* no chemisorption of Br⁻ ions on the Au surface). The presence of Br⁻ ions in the growth solution play a role in regulating the reduction potential of the metal precursor by forming [AuBr₂]⁻, which is lower than to [AuCl₂]⁻.^[31] Therefore, the role of Br⁻ ions appeared to control the reduction rate of the metal precursor via increasing or decreasing its concentration in the growth solution. The seed-mediated growth in the absence of NaBr under similar conditions yielded polyhedral or ill-defined shape Au NPs (Fig. S10 in the ESM) because the rapid reduction rate in the absence of NaBr suppressed the migration of atomic species on the surface of growing NP.

The deconvoluted high resolution XPS spectra of C1s displayed three distinct peaks. The peaks at ~ 285 eV (C-C/C-H) and ~ 286.5 eV(C-N) revealed the presence of CTAC molecules on the surface of anisotropic Au NPs (Fig. 4(a)). The presence of CTAC molecules can also be confirmed by the presence of quaternary ammonium peak at ~ 402.3 eV in N1s spectra (Fig. S11 in the ESM). A shoulder peak toward higher binding energy at ~ 288.7 eV and the peak at ~ 286.5 (C-O) suggested the presence of carboxyl (O-C = O) functional group on the surface of Au NPs. These carboxyl functional groups can be arised from AA

(ascorbic acid or ascorbate ions), indicating the existence of chemisorbed ascorbate ions along with CTAC molecules on the surface of anisotropic NPs. This peak intensity differed across all samples, and stellated Au NPs showed a clear shoulder peak (Figs. 4(d) and (e)). We determined the relative intensity ratio (%) of peak (O-C = O) to other peaks by integrating the area under the deconvoluted peaks. This ratio turned out to be low, *i.e.*, ~ 2.7%, ~ 2.6%, ~ 2.4% and ~ 2.4% for cuboctahedra (Fig. 2(b)), truncated cube (Fig. 2(c)), cube (Fig. 2(d)), and rhombic dodecahedra (Fig. 2(h)), respectively. Stellated Au NPs (Figs. 2(f) and 2(g)) showed a high ratio (~ 4.5%) compared to other shapes. The results from XPS data analysis revealed the presence of different packing density of molecules/ions across various shapes from cubic to stellated octahedron. Among different morphologies, stellated Au NPs contained relatively a higher density of AA (*i.e.* relatively high packing density of CTAC and AA on the {100} facets relative to the {111} facets) on their surfaces than other shapes. This high packing density of molecules and ions can significantly suppress the migration of atomic species from corner to flat surfaces (low surface diffusion rate). The rapid growth along the $\langle 111 \rangle$ direction, thus, facilitated the formation of stellated NPs ($V_{diffusion} \ll V_{deposition}$). A low density of AA on the surface of cuboctahedra, truncated cube, and cube Au NPs led to the overall low surface coverage of CTAC and AA on the {100} facets. As a consequence, a relatively high surface diffusion led to the formation of non-stellated Au NPs ($V_{diffusion} \gg V_{deposition}$). Therefore, the reduction rate of precursor and concentration of AA as well as the packing density of CTAC on the high energy facets play important roles in the formation of stellated Au NPs by suppressing the surface diffusion. It is also known that the reduction power of AA depends on the pH of the growth solution and increases with the increase in the pH of the growth solution. [33] The increased reduction rate of the reaction can produce excess concentration of reduced Au species which may disrupt the micellar structure of CTAC molecules on the surface of growing Au NPs. Therefore, the pH of the growth can also affect the morphology of Au NPs.

To illustrate the role of surfactant molecules CTAC and NaBr in the formation of stellated and non-stellated Au NPs, we replaced CTAC by CTAB (hexadecyltrimethylammonium bromide) and NaBr by NaCl. Au NPs were grown under identical conditions by varying the amount of 40 mM AA (75 μ L, 90 μ L and 110 μ L) in the growth solution. We noticed Au nanorods as a major reaction product and other shapes as byproducts (Figure S12 in the ESM). The shape yield of gold nanorods appeared to increase with the increase in the amount of 40 mM AA in the growth solution. However, we did not notice the formation of stellated and non-stellated Au NPs. These results indicate the role of CTAC and NaBr in the formation of stellated and non-stellated Au NPs. This can be explained based on the stability of elongated CTAB micellar structure than CTAC micellar structure, thus facilitating the formation of Au nanorods.[33]

To study the effect of seed aging on the size and morphology, we synthesized Au NPs using aged seed particles in the presence of the varied amount of AA. It should be noted that the colour of the seed solution changed from brown (1 hr) to light red (24 hrs) and dark red (96 hrs). The change in colour indicated the increase in the size of seed particles, which can have an influence on the size and morphology of NPs. When the seed solution was aged for 1 hr, the size of Au NPs increased from 76 nm to 88 nm along with the increase in the volume of 40 mM AA (75 μ L to 110 μ L) in the growth solution

(Fig. 5(a)). At a high volume of 40 mM AA (150 μ L), the size of Au NPs was measured to be 74 nm. This decrease in size can be attributed to a high rate of Au precursor reduction and the rapid consumption of Au atoms. However, we did not notice any trend in the size of anisotropic Au NPs grown by 24 hrs and 96 hrs aged seed solution in the presence of the varied amount of AA (Fig. 5(a) and Figs. S13 and S14 in the ESM). At a fixed amount of AA, an overall increase in the size of anisotropic Au NP can be seen as the aging time of seed particles increased. The seed particles aged for 96 hrs yield stellated octahedron Au NPs in the range of AA amounts (90 μ L to 110 μ L) in the growth solution (Fig. S14 in the ESM).

Au NPs display a localized surface plasmon resonance (LSPR). The position of LSPR depends on the shape and size of Au NPs, including the number of vertices and faces. To investigate the shape-dependent LSPR property of Au NPs produced in this work, ultraviolet-visible (UV-Vis) spectroscopy was used. Cuboctahedra Au NP showed a LSPR peak at around 562 nm, which can be attributed to a dipolar mode (Fig. 5(b)). As the shape of NP changed from cuboctahedra to truncated cubic, and cubic (*i.e.* the degree of truncation or the number of faces decreases), the LSPR peak was red-shifted from 562 nm to 583 nm (Fig. 5(b)). Our results are in agreement with the theoretical model that explains a red-shift in the peak with the change in the shape of Au NPs from cuboctahedra to cubes.[46] The LSPR peak was red-shifted for concave Au NP (or partially overgrown nanocube) compare to Au nanocube. As the shape of NP further evolved into octapod (612 nm) and stellated octahedra (623 nm) morphology, an additional red-shift in the LSPR peak can be seen than to cubic and concave Au NPs (Fig. 5(c)). Here, a broadening in LSPR peaks of stellated Au NPs can be attributed to the variation in the size, arm length and tip size of Au NPs. A more intense depolarizing field caused this red-shift at high charge density regions (the presence of sharp corners and edges on the concave, octapod, and stellated octahedra). The rhombic dodecahedral Au NPs showed the LSPR peak at the wavelength of 562 nm, which is blue-shifted compared to stellar Au NPs due to the absence of sharp edges and corners (Fig. 5(c)). The results from UV-vis measurements confirmed the formation of Au NPs in different morphologies.

The growth kinetics of the seed-mediated reaction depends on the type and concentration of halides. To illustrate this, we grown Au NPs in the presence of NaCl and NaBr. The growth in the presence of the varied amount of 10 mM NaCl resulted to ill-defined polyhedral morphology of Au NPs (Fig. S15 in the ESM). This uncontrolled growth of Au NPs is due to the rapid reduction rate of reaction in the presence of Cl⁻ ions (due to higher reduction potential of [AuCl₂]⁻). However, the controlled addition of NaBr to the growth solution reduces the ability of Au³⁺ to Au because Br⁻ ions strongly interact with Au precursor and thus, lower down the reduction potential of the precursor by forming [AuBr₂]⁻ complex. Au NPs were grown by varying the volume of 10 mM NaBr added to the growth solution at a fixed volume of 40 mM AA (100 μ L). The results displayed in Figs. 6(a)-(d) displayed a gradual change in the morphology of Au NP from octapod to nanocube with an increase in the amount of 10 mM NaBr in the growth solution. It can be seen that the arm length of octapod NP decreased from 54 ± 4 nm to 20 ± 3 nm with the increase in NaBr (Fig. 6(f)). Moreover, the angle between adjacent arms of octapod NP increased with the increase in the concentration of NaBr (Fig. S16 in the ESM). The quantitative yields of octapod and nanocube were determined based on a visual inspection of more than 200 NPs from different SEM images. The analysis

showed the progressive decrease in the yield of octapod from 78–9% and an increase in the yield of Au nanocubes from 22–72% as the volume of 10 mM NaBr increased from 20 μL to 70 μL in the growth solution (Fig. 6(e)). From these results, it can be learned that the addition of increased amount of 10 mM NaBr slowed down the reduction rate of reaction. This shifted the NP growth from surface controlled reaction (high reduction rate) to diffusion-controlled (low reduction rate).

For a clear description about the evolution of stellated Au NPs and other shapes, we constructed experimentally a morphology diagram based on experiments under different conditions (Fig. 7). The diagram displayed the formation of octapod Au NPs in the molar ratio of AA/Au³⁺ from 1.5 to 1.7 and NaBr concentration up to 30 μmoles . The stellated octahedron Au NPs were synthesized by adjusting the molar ratio (AA/ Au³⁺) between 1.7 and 2.1, and NaBr concentration up to 30 μmoles . The rhombic dodecahedra Au NPs were seen over a wide range of AA/Au³⁺ (above 2.1) and NaBr concentration. The other shapes, cuboctahedron, and truncated cubic NPs can be obtained at a lower molar ratio of AA/Au³⁺ (between 0.6 to 1.4). Interestingly, cubic Au NPs were emerged as a primary reaction product in the narrow molar ratio range (AA/Au³⁺~1.4–1.5) at a low concentration of NaBr. As the concentration of NaBr increased (above 30 μmoles), the cubic Au NPs can be synthesized over a wide ratio (AA/Au³⁺) range from 1.4 to 2.1. Therefore, the morphology diagram revealed the importance of AA, Au³⁺, and NaBr concentrations in the formation of stellated and non-stellated Au NPs.

Self-assembly of anisotropic Au NPs into superstructures is a promising approach to fabricate next-generation functional materials with enhanced and collective physical properties. The properties of self-assembled materials depend on the shape, orientation, and spatial arrangement of the nanoscale building blocks. In this work, we also explore the self-assembly of the stellated octahedron and rhombic dodecahedron Au NP, *i.e.*, the packing of these NPs within self-assembled superstructures. For the self-assembly, a concentrated solution of CTAC capped Au NPs was dropped on the silicon wafer (5 mm²) and left for overnight drying in a closed environment. SEM images shown in Figs. 8(a) and (b) displayed the self-assembly of stellated octahedron Au NPs. Upon close examination, different packing arrangements of the stellated Au NPs can be seen. The stellated Au NPs are packed in cubic crystal symmetry (supercrystal with {100} facets), which is the most likely the case because this configuration provides the highest structural stability as four branches per NP rest on the substrate (Fig. S17 (a) in the ESM). Another arrangement showed the packing of stellated NPs in < 111 > direction, *i.e.*, supercrystal with {111} facets. Similarly, we observed two different packing arrangements in the self-assembled rhombic dodecahedron Au NPs superstructures (Figs. 8 (c) and (d)). Assuming the cubic symmetry of supercrystals, two different arrangements can be understood based on the packing of NPs in the < 111 > and < 100 > orientations, and thereby obtained superstructures with (111) and (100) faces. The self-assembly of stellated and rhombic dodecahedron Au NPs is guided by the surfactant (CTAC) mediated interparticle depletion forces (*i.e.* the surfactant is believed to facilitate the self-assembly). [20]

The individual octapod AuNPs are expected to exhibit strong coupling with their LSPRs with the incident light field. Fig. S17 (a) in the ESM displayed a self-assembled monolayer of stellated octahedron in cubic

symmetry when the self-assembly was performed with a low concentration of NPs. Such a self-assembled superstructure can build up higher electric field enhancement due to the plasmonic hotspots at the corners or assemblies of the NPs. Thus, models were constructed to numerically investigate the distributions of electric field using FEM (finite element method). To simplify the calculations in the simulations, only short-range ordered 2×2 and 3×3 array were considered. The electric field intensity distribution has been calculated and shown in Fig. S17 (b) in the ESM (inset along the x - y plane for a single particle) and Fig. S18 in the ESM. It can be observed that the strongest enhancements are located at the plasmonic hotspots or the corners and edges of the octapod AuNPs, and these can be attributed to the plasmonic nanoantenna effect.[47] The simulations also indicate that the plasmonic enhancement is higher for a bi-layer (2×2 array) than that for monolayer or single particle arrangement. This is because there are more gaps in between the octapod Au NPs in the case of bi-layer arrangement (Fig. S18 (b) in the ESM). This property can be beneficial for surface-enhanced Raman scattering (SERS) where the Raman intensity of an analyte in the vicinity of hotspots can be enhanced drastically.

3. Conclusions

We demonstrated a simple seed-mediated approach to grow stellated and non-stellated anisotropic Au NPs in high yield. This work sheds new light on the crucial link between the reduction rate of reaction (controlled by the concentration of AA and NaBr) and the morphology of NPs. At a low reduction rate (low supersaturation), the diffusion-controlled growth led to thermodynamically stabilized cuboctahedron and truncated cubic Au NPs. At a moderate reduction rate, the surface controlled growth ($V_{deposition} \sim V_{diffusion}$) dominated and facilitated the growth of cubic Au NPs. By adjusting the $V_{deposition} \gg V_{diffusion}$ via increasing the reduction rate and supersaturation, the rapid deposition of Au atoms along the $\langle 111 \rangle$ direction favored the kinetically stabilized stellated Au NPs in high yield. Experimental and computer simulations results revealed the stability of stellated Au NPs upto 500K. A sufficiently high reduction rate resulted in the growth of rhombic dodecahedron Au NPs. The size and morphology of anisotropic Au NPs can be tailored by varying the aging time of seed particles. Furthermore, the results revealed that the size and morphology of stellated Au NPs can be controlled via the concentration of NaBr, which influences the reduction rate of the metal precursor as well as the surface processes ($V_{deposition}, V_{diffusion}$). A morphology diagram, for the first time, was constructed, allowing us to design stellated and non-stellated Au NPs in high yield. The stellated and rhombic dodecahedron Au NPs can be self-assembled into superstructures possessing cubic symmetry. Theoretical calculations showed the plasmonic enhancement effect in 2D self-assembled superstructures fabricated from stellated Au NPs in cubic symmetry. Overall, this work provides a rational strategy for synthesizing stellated and other anisotropic Au NPs with simultaneous improvement in the yield and monodispersity and size tunability.

4. Experimental

Materials. Gold (III) chloride trihydrate ($\text{HAuCl}_4 \cdot 3\text{H}_2\text{O}$, $\geq 99.9\%$ trace metals basis), L-ascorbic acid (BioXtra, $\geq 99.0\%$, crystalline), sodium borohydride (NaBH_4 , powder, $\geq 98.0\%$), cetyltrimethylammonium

chloride solution (CTAC, 25 wt. % in H₂O), sodium bromide (NaBr, ACS reagent, ≥ 99.0%) and Poly(ethylene glycol) methyl ether thiol were purchased from Sigma Aldrich.

Preparation of Au seed particles. We prepared a total of 10 mL aqueous solution containing 0.25 mM HAuCl₄ (250 μL from 10 mM HAuCl₄) and 100 mM CTAC (1.28 mL from a stock solution of 781 mM CTAC), and deionized water (8.672 mL). The solution was kept for stirring at 800 rpm for 2 min at room temperature. A 450 μL from freshly prepared NaBH₄ solution of 20 mM (7.57 mg in 10 mL deionized water) was rapidly added to the 10 mL solution. The colour of the solution was immediately turned to brown, indicating the formation of Au seed particles. The solution was kept under stirring at 800 rpm for 2 min and left at room temperature for 1 hr.

Synthesis of anisotropic Au nanoparticles. To grow anisotropic Au nanoparticles, we prepared two growth solutions (total volume 10 mL in each of the two glass vials). To grow cuboctahedron Au NPs, 1.28 mL of 781 mM CTAC, 0.25 mL of 10 mM HAuCl₄, 10 μL of 10 mM NaBr, and 75 μL of 40 mM AA (ascorbic acid) was added to deionized water (8.385 mL). The concentration of CTAC and HAuCl₄ in the final solution was determined to be 100 mM and 0.25 mM, respectively. A yellow growth solution turned to colorless after adding AA to the growth solution, indicating the reduction of Au³⁺ to Au⁺. The glass vials were kept in a water bath set at 30°C. A 25 μL from the seed solution was transferred to the first growth solution and shake. As soon as the color of the first growth solution changed to light pink (within 5-15s depending on the volume of 40 mM AA added to the growth solution), 25 μL seed solution from the first growth solution was immediately transferred to a second growth solution. The reaction was left for 20 min at 30°C. The nanoparticle solution centrifuged twice at 2500 rpm for 10 min to remove the excess of surfactant molecules. The final reaction product was dispersed in 2 mL deionized water. The experimental conditions for synthesizing various anisotropic Au nanoparticles are illustrated in Table S1. All experiments were performed at pH = 6.5.

Characterization techniques. Scanning electron microscopy (SEM, Carl Zeiss Sigma HD) operating at 5 kV was used to collect images of anisotropic Au nanoparticles. Samples for TEM investigation were prepared by evaporating a few μL of nanoparticle solution on a silicon wafer (5 mm²). Ultraviolet - visible (UV - vis) absorption spectroscopy of anisotropic Au nanoparticles was performed using a FLUOstar Omega (200–1100 nm). X-ray photoelectron spectroscopy technique (Thermo Fisher Scientific K-Alpha) was used to probe the surface chemistry and composition of anisotropic Au nanoparticles. Samples for SEM and XPS analysis were prepared by evaporating a few μL of nanoparticle solution on a silicon wafer (5 mm²).

Finite element method (FEM) calculations. To investigate the behavior of the octapod gold nanoparticles (AuNPs) on excitation of light, numerical calculations were performed using the commercial software package (Comsol Multiphysics 5.3). The electromagnetic properties of the octapod AuNPs were handled by the finite element method (FEM) by selecting the spatial grid appropriately. The frequency dependent dielectric function of bulk Au from the experimental results of Johnson and Christy was used in the calculations.[48] The surrounding medium is presumed to be air with a refractive index as 1.0.

Declarations

Acknowledgements

The authors gratefully acknowledge the financial support of the Australian Research Council and the Australian National Health and Medical Research Council. The authors acknowledge the Australian Centre for Microscopy and Microanalysis, and the Sydney Nano, University of Sydney with technical support for the materials characterization. Authors would like to thank IITM-UniSyd Global alliance for partial research support.

Electronic Supplementary Material: Additional detail on molecular dynamic simulation used in the study, SEM images, Tables and XPS data.

References

1. Bandyopadhyay, S.;McDonagh, B. H.;Singh, G.;Raghunathan, K.;Sandvig, A.;Sandvig, I.;Andreassen, J. P.; Glomm, W. R. Growing gold nanostructures for shape-selective cellular uptake. *Nanoscale Res. Lett.* 2018, *13*, 254–266.
2. Dong, Y. C.;Hajfathalian, M.;Maidment, P. S. N.;Hsu, J. C.;Naha, P. C.;Si-Mohamed, S.;Breuilly, M.;Kim, J.;Chhour, P.;Douek, P.;Litt, H. I.; Cormode, D. P. Effect of Gold Nanoparticle Size on Their Properties as Contrast Agents for Computed Tomography. *Sci. Rep.* 2019, *9*, 14912–14925.
3. Fleury, B.;Cortes-Huerto, R.;Tache, O.;Testard, F.;Menguy, N.; Spalla, O. Gold Nanoparticle Internal Structure and Symmetry Probed by Unified Small-Angle X-ray Scattering and X-ray Diffraction Coupled with Molecular Dynamics Analysis. *Nano Lett.* 2015, *15*, 6088–6094.
4. Gong, N.;Chen, S.;Jin, S.;Zhang, J.;Wang, P. C.; Liang, X. J. Effects of the physicochemical properties of gold nanostructures on cellular internalization. *Regen. Biomater.* 2015, *2*, 273–280.
5. He, Y.;Liu, J. C.;Luo, L.;Wang, Y. G.;Zhu, J.;Du, Y.;Li, J.;Mao, S. X.; Wang, C. Size-dependent dynamic structures of supported gold nanoparticles in CO oxidation reaction condition. *Proc. Natl. Acad. Sci. U S A* 2018, *115*, 7700–7705.
6. Xia, Y.;Xiong, Y.;Lim, B.; Skrabalak, S. E. Shape-controlled synthesis of metal nanocrystals: simple chemistry meets complex physics? *Angew. Chem. Int. Ed. Engl.* 2009, *48*, 60–103.
7. Priecel, P.;Salami, H. A.;Padilla, R. H.;Zhong, Z. Y.; Lopez-Sanchez, J. A. Anisotropic gold nanoparticles: Preparation and applications in catalysis. *Chin. J. Catal.* 2016, *37*, 1619–1650.
8. Lim, W. Q.; Gao, Z. Q. Plasmonic nanoparticles in biomedicine. *Nano Today* 2016, *11*, 168–188.
9. Kohout, C.;Santi, C.; Polito, L. Anisotropic Gold Nanoparticles in Biomedical Applications. *Int. J. Mol. Sci.* 2018, *19*, 3385–3415.
10. Toy, R.;Hayden, E.;Shoup, C.;Baskaran, H.; Karathanasis, E. The effects of particle size, density and shape on margination of nanoparticles in microcirculation. *Nanotechnol.* 2011, *22*, 115101–115110.

11. Gentile, F.;Chiappini, C.;Fine, D.;Bhavane, R. C.;Peluccio, M. S.;Cheng, M. M. C.;Liu, X.;Ferrari, M.; Decuzzi, P. The effect of shape on the margination dynamics of non-neutrally buoyant particles in two-dimensional shear flows. *J. Biomech.* 2008, *41*, 2312–2318.
12. Kolhar, P.;Anselmo, A. C.;Gupta, V.;Pant, K.;Prabhakarapandian, B.;Ruoslahti, E.; Mitragotri, S. Using shape effects to target antibody-coated nanoparticles to lung and brain endothelium. *Proc. Natl. Acad. Sci. U S A* 2013, *110*, 10753–10758.
13. Muro, S.;Garnacho, C.;Champion, J. A.;Leferovich, J.;Gajewski, C.;Schuchman, E. H.;Mitragotri, S.; Muzykantov, V. R. Control of endothelial targeting and intracellular delivery of therapeutic enzymes by modulating the size and shape of ICAM-1-targeted carriers. *Mol. Therapy* 2008, *16*, 1450–1458.
14. Geng, Y.;Dalhaimer, P.;Cai, S. S.;Tsai, R.;Tewari, M.;Minko, T.; Discher, D. E. Shape effects of filaments versus spherical particles in flow and drug delivery. *Nat. Nanotechnol.* 2007, *2*, 249–255.
15. Arnida;Janat-Amsbury, M. M.;Ray, A.;Peterson, C. M.; Ghandehari, H. Geometry and surface characteristics of gold nanoparticles influence their biodistribution and uptake by macrophages. *Eur. J. Pharma. Biopharma.* 2011, *77*, 417–423.
16. Champion, J. A.; Mitragotri, S. Role of target geometry in phagocytosis. *Proc. Natl. Acad. Sci. U S A* 2006, *103*, 4930–4934.
17. Yue, J.;Feliciano, T. J.;Li, W.;Lee, A.; Odom, T. W. Gold Nanoparticle Size and Shape Effects on Cellular Uptake and Intracellular Distribution of siRNA Nanoconstructs. *Bioconjugate Chem.* 2017, *28*, 1791–1800.
18. Smith, B. R.;Kempen, P.;Bouley, D.;Xu, A.;Liu, Z.;Melosh, N.;Dai, H. J.;Sinclair, R.; Gambhir, S. S. Shape Matters: Intravital Microscopy Reveals Surprising Geometrical Dependence for Nanoparticles in Tumor Models of Extravasation. *Nano Lett.* 2012, *12*, 3369–3377.
19. Peiris, P. M.;Toy, R.;Doolittle, E.;Pansky, J.;Abramowski, A.;Tam, M.;Vicente, P.;Tran, E.;Hayden, E.;Camann, A.;Mayer, A.;Erokwu, B. O.;Berman, Z.;Wilson, D.;Baskaran, H.;Flask, C. A.;Keri, R. A.; Karathanasis, E. Imaging Metastasis Using an Integrin-Targeting Chain-Shaped Nanoparticle. *ACS Nano* 2012, *6*, 8783–8795.
20. Peiris, P. M.;Bauer, L.;Toy, R.;Tran, E.;Pansky, J.;Doolittle, E.;Schmidt, E.;Hayden, E.;Mayer, A.;Keri, R. A.;Griswold, M. A.; Karathanasis, E. Enhanced Delivery of Chemotherapy to Tumors Using a Multicomponent Nanochain with Radio-Frequency-Tunable Drug Release. *ACS Nano* 2012, *6*, 4157–4168.
21. Barua, S.;Yoo, J. W.;Kolhar, P.;Wakankar, A.;Gokarn, Y. R.; Mitragotri, S. Particle shape enhances specificity of antibody-displaying nanoparticles. *Proc. Natl. Acad. Sci. U S A* 2013, *110*, 3270–3275.
22. Toy, R.;Peiris, P. M.;Ghaghada, K. B.; Karathanasis, E. Shaping cancer nanomedicine: the effect of particle shape on the in vivo journey of nanoparticles. *Nanomedicine* 2013, *9*, 121–134.
23. Singh, G.;van Helvoort, A. T. J.;Bandyopadhyay, S.;Volden, S.;Andreassen, J.-P.; Glomm, W. R. Synthesis of Au nanowires with controlled morphological and structural characteristics. *Appl. Surf. Sci.* 2014, *311*, 780–788.

24. Chang, Y.-X.;Zhang, N.-N.;Xing, Y.-C.;Zhang, Q.;Oh, A.;Gao, H.-M.;Zhu, Y.;Baik, H.;Kim, B.;Yang, Y.;Chang, W.-S.;Sun, T.;Zhang, J.;Lu, Z.-Y.;Lee, K.;Link, S.; Liu, K. Gold Nanotetrapods with Unique Topological Structure and Ultranarrow Plasmonic Band as Multifunctional Therapeutic Agents. *J. Phys. Chem. Lett.* 2019, *10*, 4505–4510.
25. Chen, S.;Wang, Z. L.;Ballato, J.;Foulger, S. H.; Carroll, D. L. Monopod, bipod, tripod, and tetrapod gold nanocrystals. *J Am Chem Soc* 2003, *125*, 16186–16187.
26. Sánchez-Iglesias, A.;Winckelmans, N.;Altantzis, T.;Bals, S.;Grzelczak, M.; Liz-Marzán, L. M. High-Yield Seeded Growth of Monodisperse Pentatwinned Gold Nanoparticles through Thermally Induced Seed Twinning. *J. Am. Chem. Soc.* 2017, *139*, 107–110.
27. Zheng, Y.;Liu, W.;Lv, T.;Luo, M.;Hu, H.;Lu, P.;Choi, S. I.;Zhang, C.;Tao, J.;Zhu, Y.;Li, Z. Y.; Xia, Y. Seed-mediated synthesis of gold tetrahedra in high purity and with tunable, well-controlled sizes. *Chem. Asian J.* 2014, *9*, 2635–2640.
28. Chen, L.;Ji, F.;Xu, Y.;He, L.;Mi, Y.;Bao, F.;Sun, B.;Zhang, X.; Zhang, Q. High-Yield Seedless Synthesis of Triangular Gold Nanoplates through Oxidative Etching. *Nano Lett.* 2014, *14*, 7201–7206.
29. Kuo, B.-H.;Hsia, C.-F.;Chen, T.-N.; Huang, M. H. Systematic Shape Evolution of Gold Nanocrystals Achieved through Adjustment in the Amount of HAuCl₄ Solution Used. *J. Phys. Chem. C* 2018, *122*, 25118–25126.
30. Bandyopadhyay, S.;Singh, G.; Glomm, W. R. Shape tunable synthesis of anisotropic gold nanostructures through binary surfactant mixtures. *Mater. Today Chem.* 2017, *3*, 1–9.
31. Langille, M. R.;Personick, M. L.;Zhang, J.; Mirkin, C. A. Defining rules for the shape evolution of gold nanoparticles. *J. Am. Chem. Soc.* 2012, *134*, 14542–14554.
32. Langille, M. R.;Personick, M. L.;Zhang, J.; Mirkin, C. A. Defining Rules for the Shape Evolution of Gold Nanoparticles. *J. Am. Chem. Soc.* 2012, *134*, 14542–14554.
33. Harper-Harris, J.;Kant, K.; Singh, G. Oleic Acid-Assisted Synthesis of Tunable High-Aspect-Ratio Multiply-Twinned Gold Nanorods for Bioimaging. *ACS Appl. Nano Mater.* 2021, *4*, 3325–3330.
34. Ahn, H.-Y.;Lee, H.-E.;Jin, K.; Nam, K. T. Extended gold nano-morphology diagram: synthesis of rhombic dodecahedra using CTAB and ascorbic acid. *J. Mater. Chem. C* 2013, *1*, 6861–6868.
35. Ye, E.;Regulacio, M. D.;Zhang, S. Y.;Loh, X. J.; Han, M. Y. Anisotropically branched metal nanostructures. *Chem. Soc. Rev.* 2015, *44*, 6001–6017.
36. Chang, Y. X.;Gao, H. M.;Zhang, N. N.;Tao, X. F.;Sun, T.;Zhang, J.;Lu, Z. Y.;Liu, K.; Yang, B. Synergistic Reducing Effect for Synthesis of Well-Defined Au Nanooctopods With Ultra-Narrow Plasmon Band Width and High Photothermal Conversion Efficiency. *Front. Chem.* 2018, *6*, 335.
37. Weiner, R. G.;Kunz, M. R.; Skrabalak, S. E. Seeding a New Kind of Garden: Synthesis of Architecturally Defined Multimetallic Nanostructures by Seed-Mediated Co-Reduction. *Acc. Chem. Res.* 2015, *48*, 2688–2695.
38. Desantis, C. J.;Peeverly, A. A.;Peters, D. G.; Skrabalak, S. E. Octopods versus concave nanocrystals: control of morphology by manipulating the kinetics of seeded growth via co-reduction. *Nano Lett.* 2011, *11*, 2164–2168.

39. DeSantis, C. J.;Sue, A. C.;Bower, M. M.; Skrabalak, S. E. Seed-mediated co-reduction: a versatile route to architecturally controlled bimetallic nanostructures. *ACS Nano* 2012, *6*, 2617–2628.
40. Iavicoli, I.;Farina, M.;Fontana, L.;Lucchetti, D.;Leso, V.;Fanali, C.;Cufino, V.;Boninsegna, A.;Leopold, K.;Schindl, R.;Brucker, D.; Sgambato, A. In vitro evaluation of the potential toxic effects of palladium nanoparticles on fibroblasts and lung epithelial cells. *Toxicol. in Vitro* 2017, *42*, 191–199.
41. Leso, V.; Iavicoli, I. Palladium Nanoparticles: Toxicological Effects and Potential Implications for Occupational Risk Assessment. *Int. J. Mol. Sci.* 2018, *19*, 503–522.
42. Walsh, M. J.;Barrow, S. J.;Tong, W. M.;Funston, A. M.; Etheridge, J. Symmetry Breaking and Silver in Gold Nanorod Growth. *ACS Nano* 2015, *9*, 715–724.
43. Njoki, P. N.;Luo, J.;Kamundi, M. M.;Lim, S.; Zhong, C. J. Aggregative Growth in the Size-Controlled Growth of Monodispersed Gold Nanoparticles. *Langmuir* 2010, *26*, 13622–13629.
44. Barmparis, G. D.;Lodziana, Z.;Lopez, N.; Remediakis, I. N. Nanoparticle shapes by using Wulff constructions and first-principles calculations. *Beilstein J. Nanotechnol.* 2015, *6*, 361–368.
45. Wen, Y.-N.; Zhang, J.-M. Surface energy calculation of the fcc metals by using the MAEAM. *Solid State Commun.* 2007, *144*, 163–167.
46. Noguez, C. Surface Plasmons on Metal Nanoparticles: The Influence of Shape and Physical Environment. *J. Phys. Chem. C* 2007, *111*, 3806–3819.
47. Marqués-González, S.;Matsushita, R.; Kiguchi, M. Surface enhanced Raman scattering of molecules in metallic nanogaps. *J. Optics* 2015, *17*, 114001.
48. Johnson, P. B.; Christy, R. W. Optical Constants of the Noble Metals. *Phys. Rev. B* 1972, *6*, 4370–4379.

Tables

Table 1 Rate constant (k) and critical growth exponent (n) derived from the fitting of absorbance-time data collected (Fig. S6 in the ESM) for various anisotropic Au NPs synthesized in the presence of varying amount of AA.

Amount of 40 mM ascorbic acid (AA) in the growth solution	Rate constant (k)	Critical growth exponent (n)
75 μ L	2.1×10^{-2}	1.8
80 μ L	2.5×10^{-2}	1.8
90 μ L	2.9×10^{-2}	1.6
100 μ L	3.1×10^{-2}	1.7
110 μ L	3.8×10^{-2}	1.6
150 μ L	4.7×10^{-2}	1.5

Figures

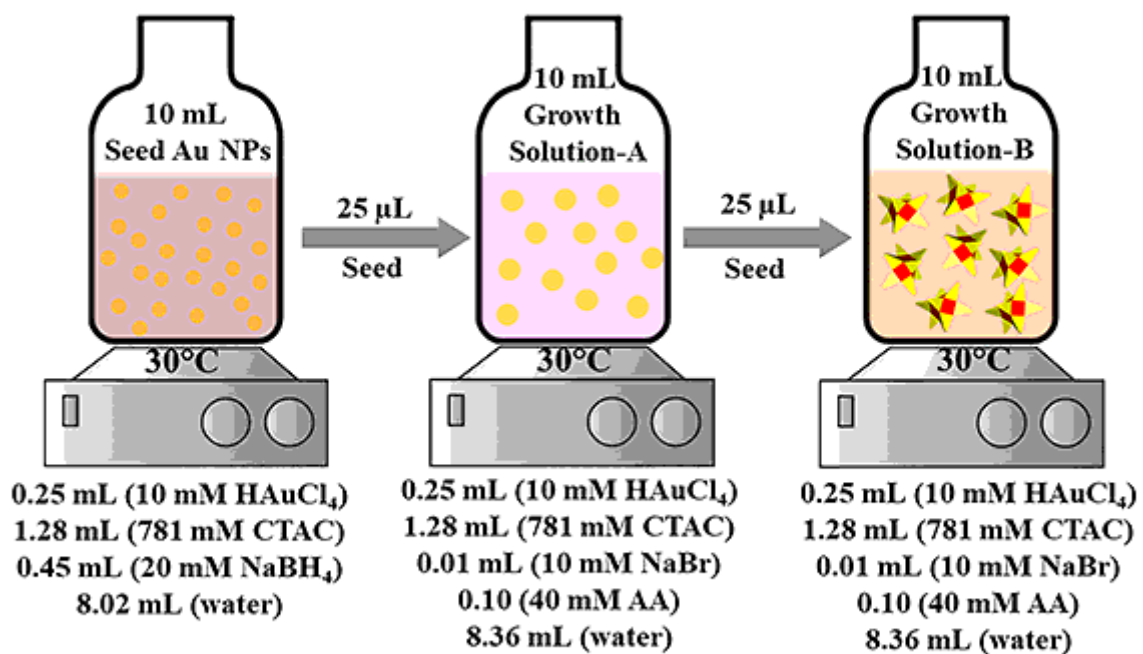


Figure 1

Experimental illustration for synthesizing anisotropic Au NPs via a seed-mediated strategy.

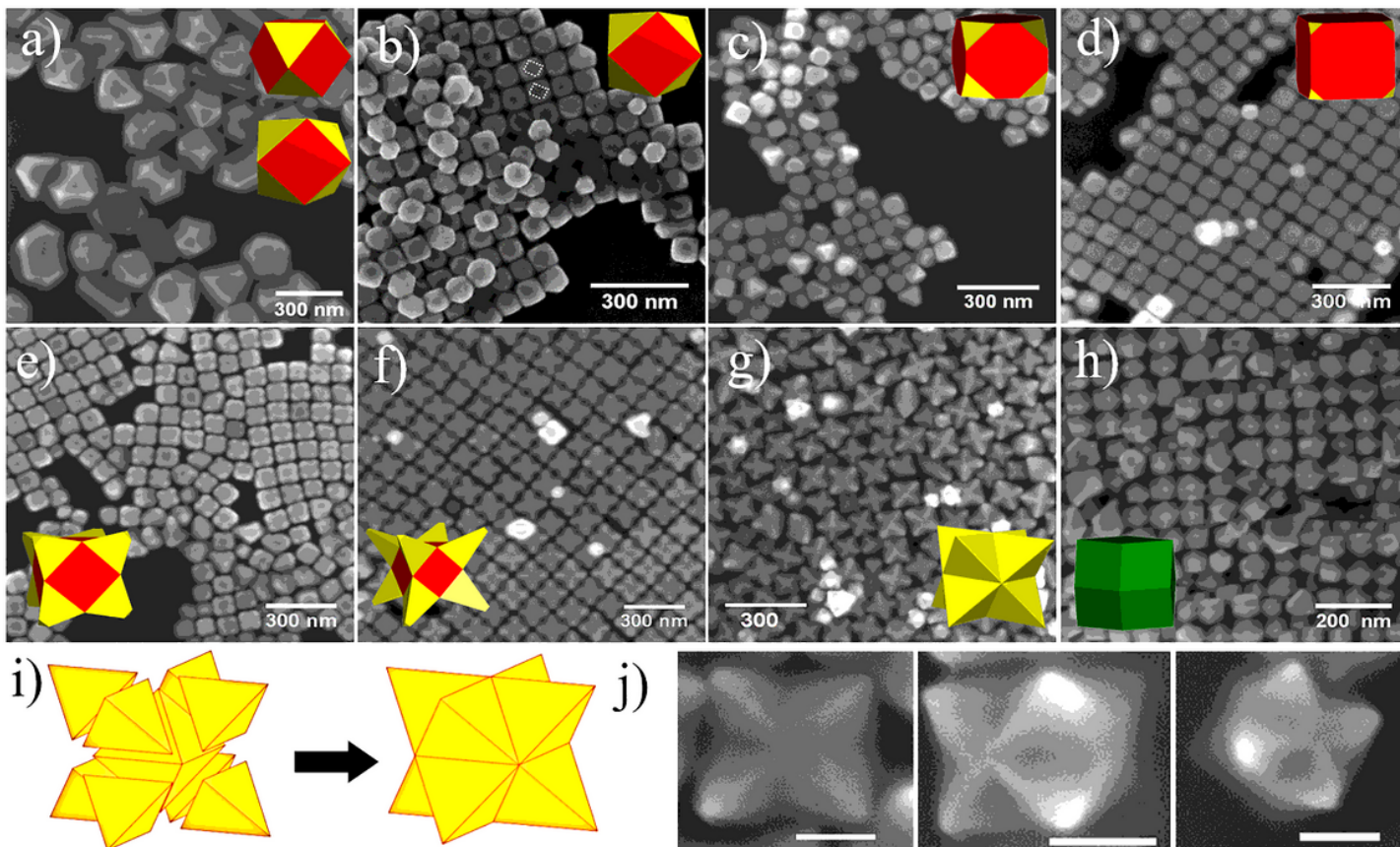


Figure 2

SEM images show the evolution of different shapes of Au NPs with increasing volume of 40 mM AA (reducing agent) to the growth solution; (a) 60 μL ; (b) 75 μL , size = 76 ± 5 nm; (c) 80 μL , size = 66 ± 7 nm; (d) 90 μL , size = 84 ± 5 nm; (e) 95 μL , size = 75 ± 6 nm; (f) 100 μL , size = 86 ± 5 nm; (g) 110 μL , size = 88 ± 6 nm and (h) 150 μL , size = 74 ± 7 nm. (i) The illustration displays the formation of stellated octahedron morphology by eight tetrahedra on each face of octahedra. (j) SEM images taken from different angles confirm the formation stellated octahedron morphology of Au NP. Scale bar: 20 nm.

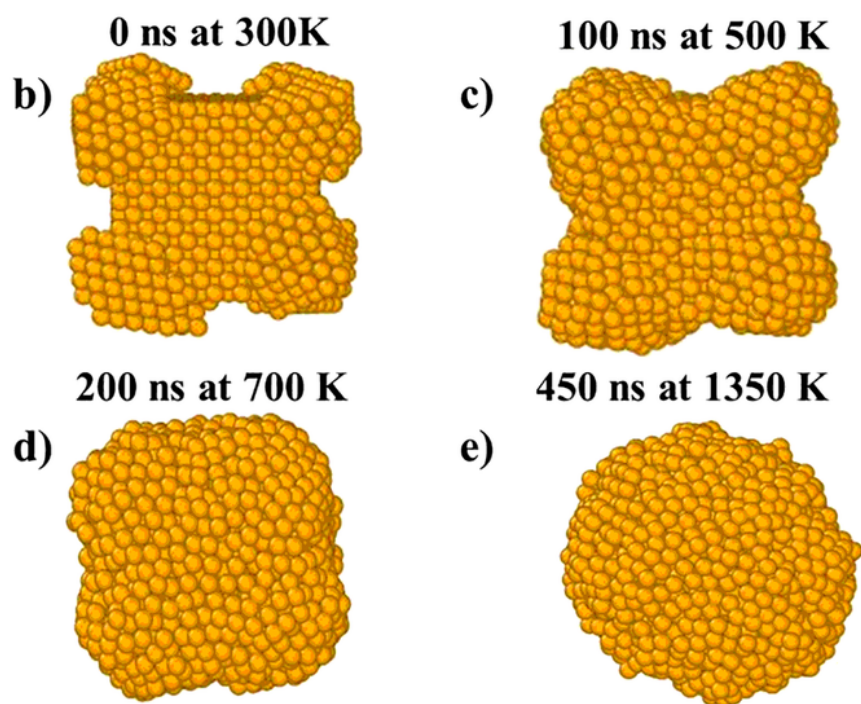
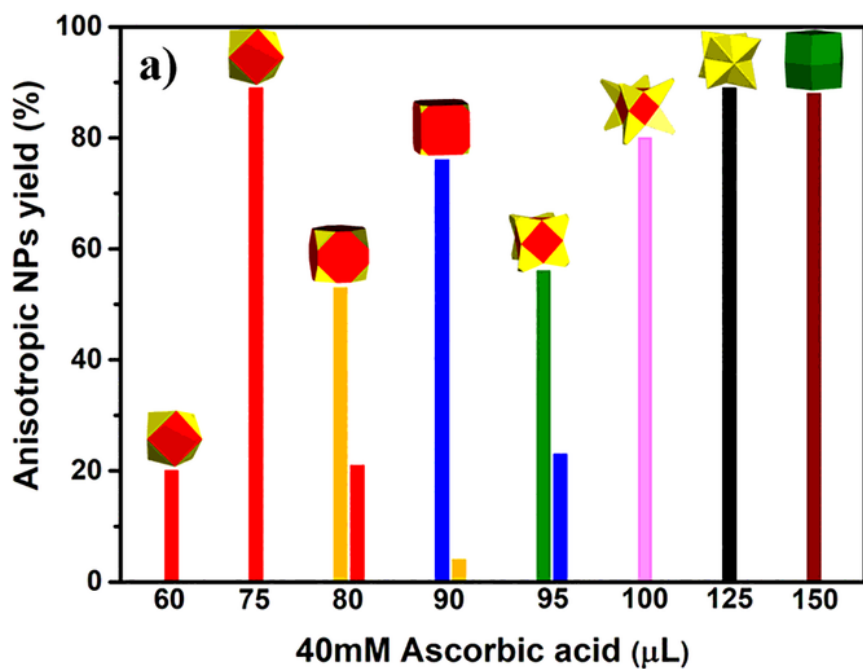


Figure 3

a) The quantitative yield (%) determination of various shaped Au NPs formed at different volume of 40 mM AA based on SEM images. MD simulations show the stability of stellated Au NP at different timesteps of relaxation; b) 0 ns at 300K, c) 100 ns at 500 K, d) 200 ns at 700K and e) 450 ns at 1350 K.

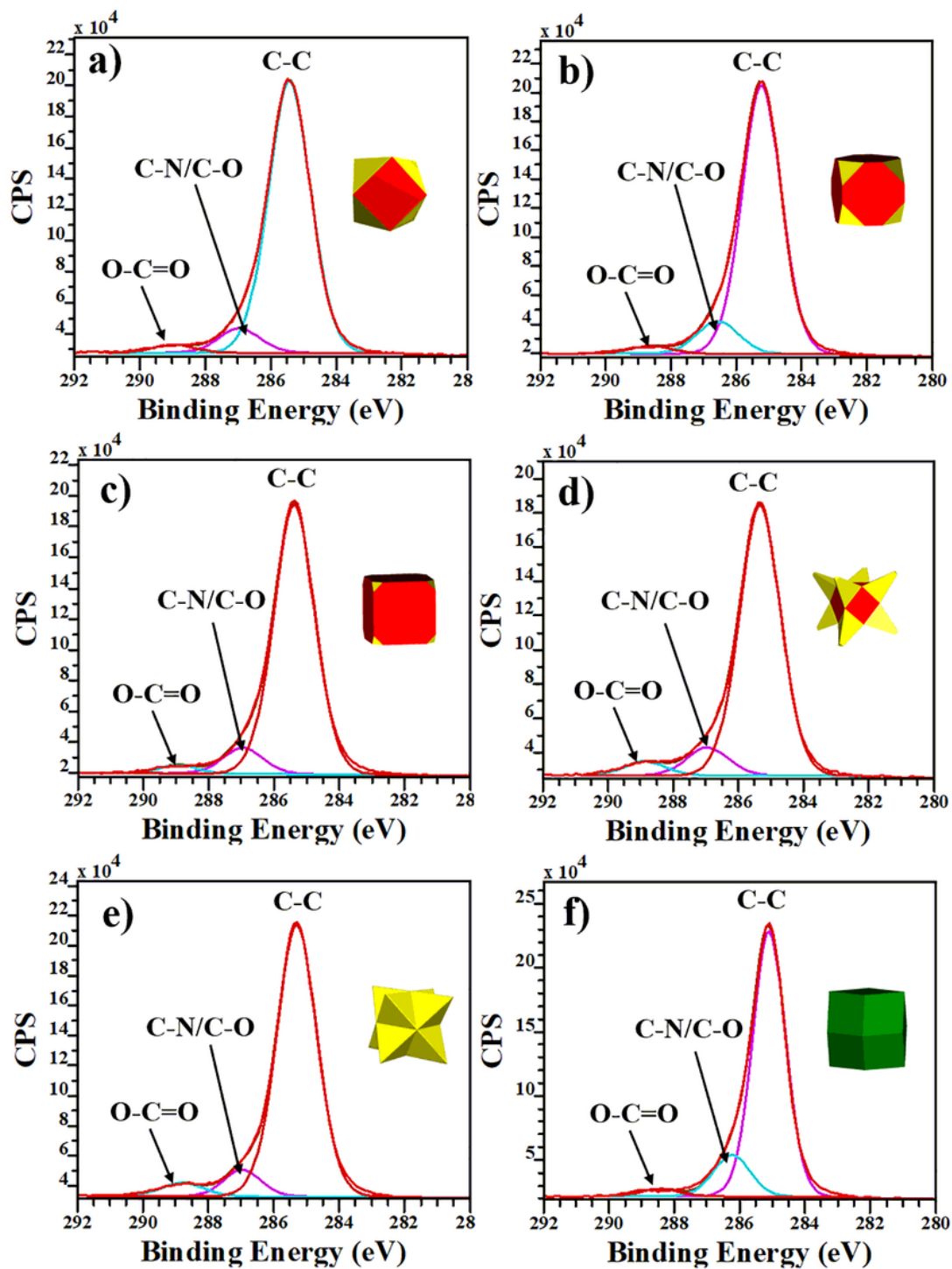


Figure 4

High resolution XPS spectra of C1s acquired from anisotropic Au NPs shown in (a) Fig. 2b, (b) Fig. 2c, (c) Fig. 2(d), (d) Fig. 2(f), (e) Fig. 2(g) and (f) Fig. 2(h).

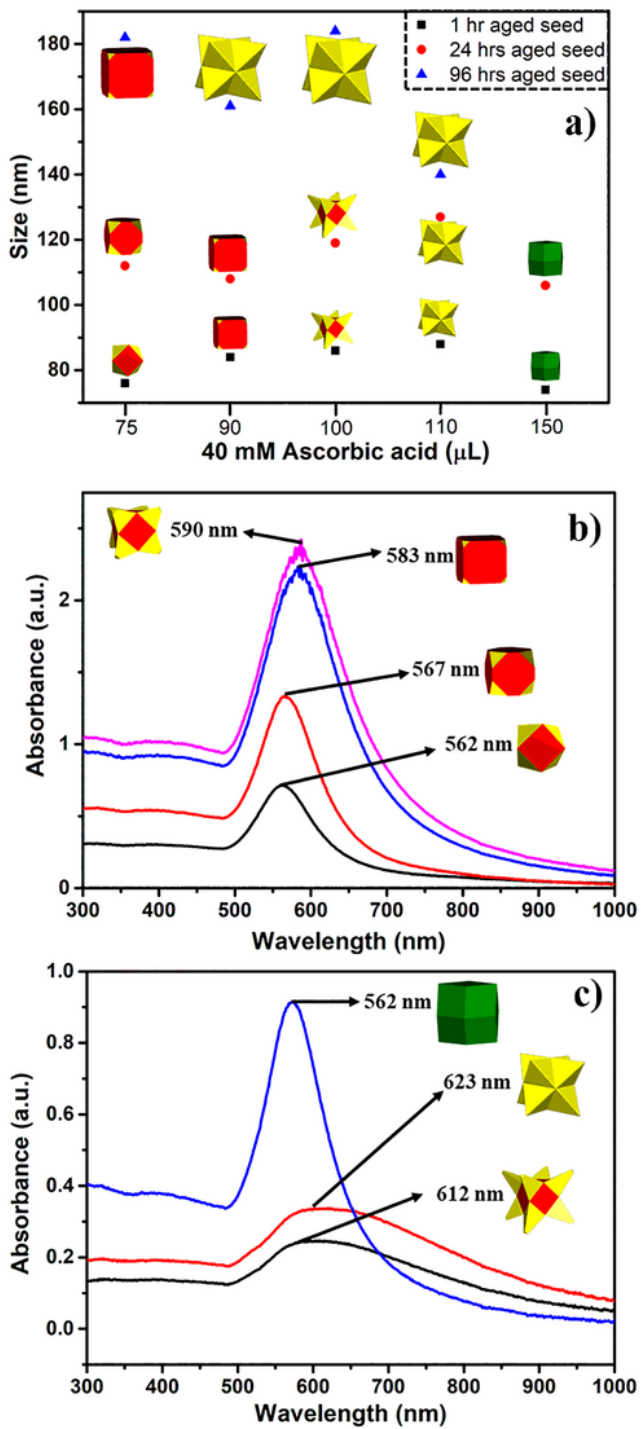


Figure 5

(a) The plot shows the variation in the size and morphology of Au NPs along with varied amount of 40 mM AA by using seed aged for different time. (b, c) The shape dependent plasmonic properties of Au NPs measured by UV-vis spectroscopy.

Increasing volume of 10 mM NaBr →

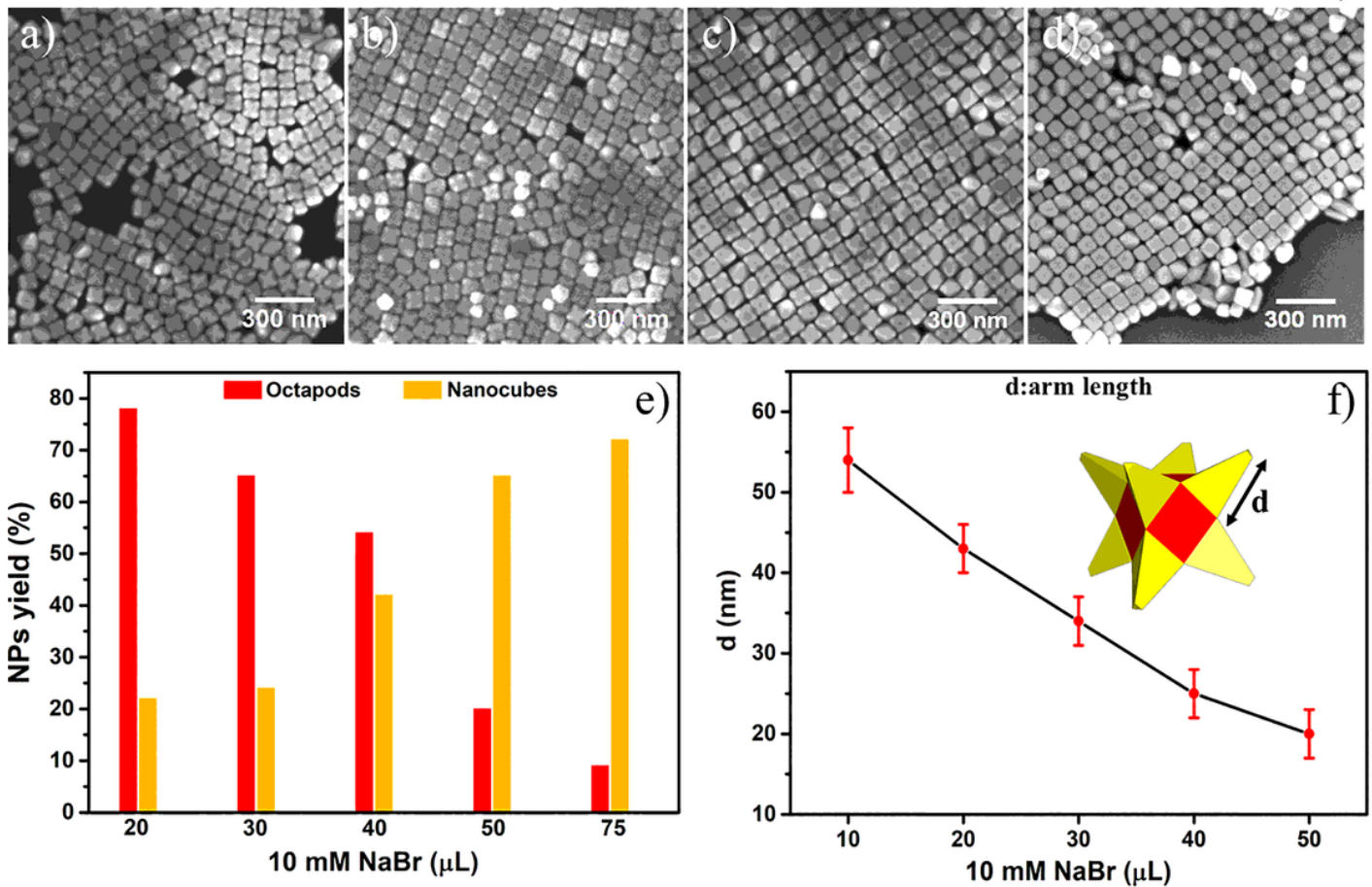


Figure 6

The influence of 10 mM NaBr amount on the morphology, yield, and size of octapod Au NPs. SEM images show a gradual change in the morphology of Au NPs from octapod to cubic as the volume of 10 mM NaBr increase in the growth solution; (a) 20 μL , (b) 30 μL , (c) 40 μL , and (d) 75 μL . (e) The quantitative yield of octapod NP decreases along with the increase in the volume of 10 mM NaBr (the yield of nanocube increases). (f) The variation in the size (arm length) of octapod Au NPs with increasing amount of 10 mM NaBr.

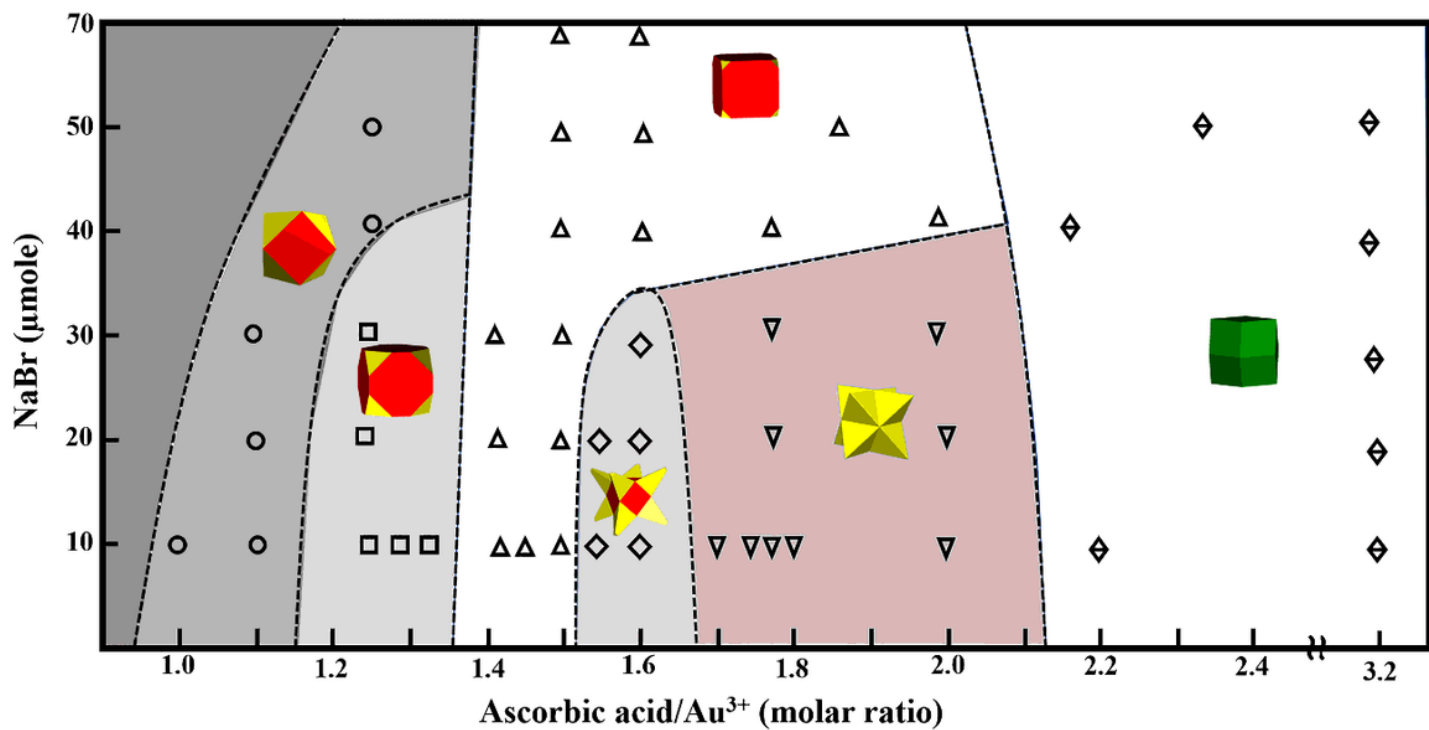


Figure 7

Morphology phase diagram displays the formation of different anisotropic Au NPs with varying concentrations of NaBr and AA/Au³⁺ molar ratio in the growth solution.

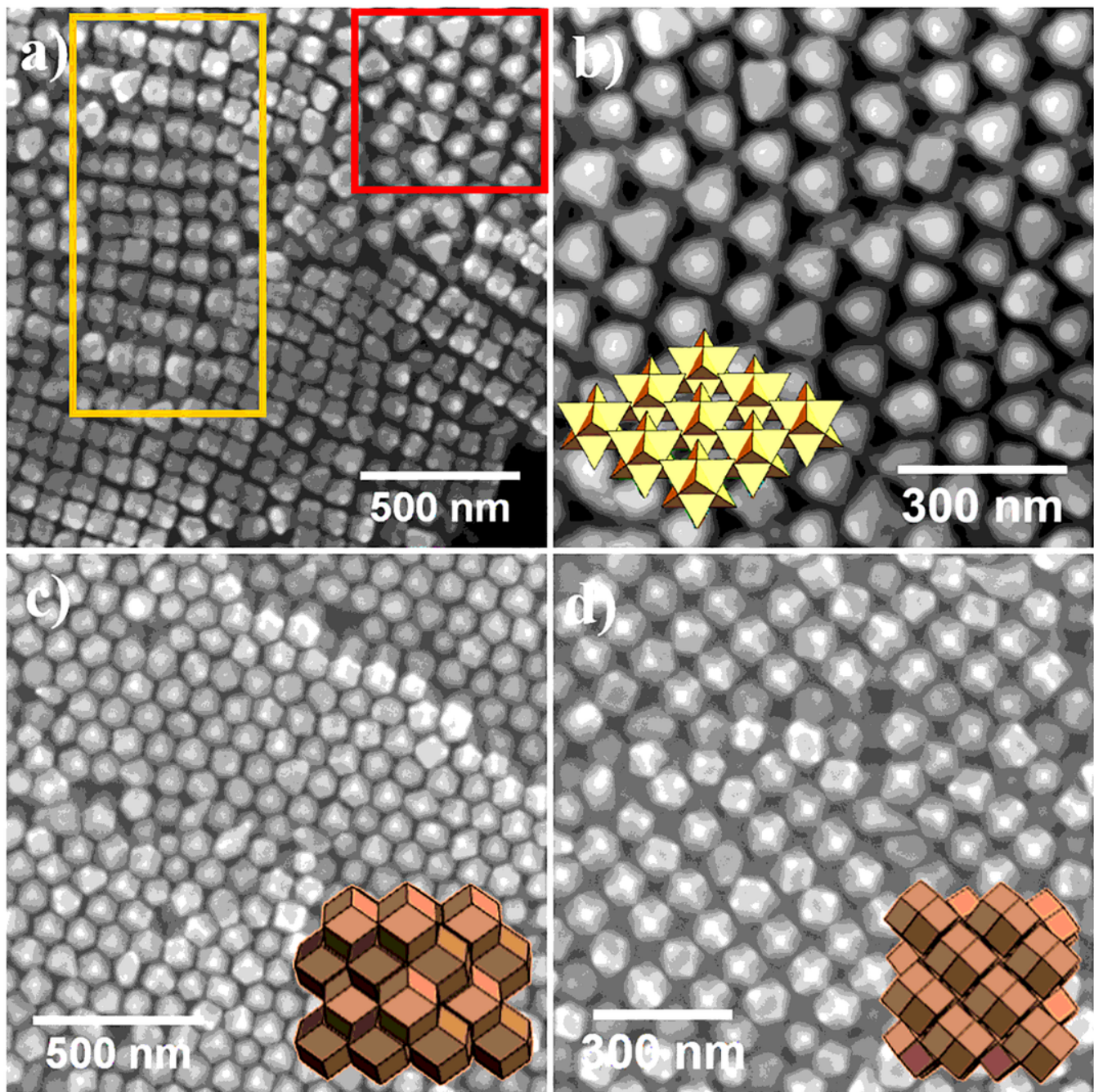


Figure 8

(a) SEM image of stellated octahedron Au NPs self-assembled into superstructures of different orientation. Red and yellow regions represent the $\{111\}$ and $\{110\}$ faces of the assembled crystals, and remaining area is the $\{100\}$ faces. (b) Magnified view of $\{111\}$ face of self-assembled supercrystals. SEM images display the self-assembly of rhombic dodecahedra Au NPs in supercrystals with the (c) $\{111\}$ face and (d) $\{100\}$ faces.

Supplementary Files

This is a list of supplementary files associated with this preprint. Click to download.

- [TOCGraphic.docx](#)
- [MovieS1.mp4](#)
- [SupportingInformation.pdf](#)